Electric Power Systems Research 163 (2018) 18–27

Contents lists available at ScienceDirect

Electric Power Systems Research

journal homepage: www.elsevier.com/locate/epsr

Thermal and electrical performance assessments of lithium-ion battery modules for an electric vehicle under actual drive cycles

S. Panchal[a,*], M. Mathew[c], I. Dincer[a], M. Agelin-Chaab[a], R. Fraser[b], M. Fowler[c]

[a] Department of Automotive, Mechanical & Manufacturing Engineering, Faculty of Engineering & Applied Science University of Ontario Institute of Technology, 2000 Simcoe Street North, Oshawa, Ontario, L1H 7K4, Canada

[b] Mechanical and Mechatronic Engineering Department, University of Waterloo, 200 University Avenue West, Waterloo, Ontario, N2L 3G1, Canada

[c] Chemical Engineering Departments, University of Waterloo, 200 University Avenue West, Waterloo, Ontario, N2L 3G1, Canada

ARTICLE INFO

Keywords:
Lithium-ion battery
Electric vehicle
Drive cycle
Temperature distribution
State of charge
Neural network

ABSTRACT

In this paper, both thermal and electrical performance evaluations of a lithium-ion battery pack using real world drive cycles from an electric vehicle (EV) are presented. For the experimental measurements, a data logger is installed in the EV, and the real world drive cycles are collected. The EV has three lithium-ion battery packs consisting of a total of 20 battery modules in series. Each module contains six series × 49 parallel IFR 18650 cylindrical valence cells. The reported drive cycles consist of different modes: acceleration, constant speed, and deceleration in both highway and city driving at 2 °C, 10 °C and 17 °C ambient temperatures with all accessories on. Later, the same drive cycles are conducted in an experimental facility where four cylindrical lithium-ion cells are connected in series, and both electrical and thermal performances are evaluated. In addition, the battery model is developed using artificial neural network, which is validated with the real world drive cycles. The validation is carried out in terms of voltage, state of charge (SOC), and temperature profiles for all the collected drive cycles. The present model closely estimates the profiles observed in the experimental data. Moreover, with this study, the mathematical function for the average temperature, SOC, and voltage prediction are developed with weights and bias values.

1. Introduction

Automotive manufacturers are under extreme pressure to improve fuel economy and reduce emissions of their cars. In conjunction with this, they have to create and apply recent advancements to meet regulations. Electric vehicles (EVs), along with fuel cell vehicles (FCVs) and hybrid electric vehicles (HEVs), are seen as the answer to energy and environmental issues and they are more energy proficient [1,2]. In EVs, since the electric motors and inverters are utilized in the drive systems, in comparison with internal combustion engines, they have real points of interest. For example, fast torque reaction and control over every wheel [3]. The heart of EVs is the battery or battery pack. Among accessible technologies, the lithium-ion battery plays a key part in the improvement of EVs, HEVs, and PHEVs [4] as a result of their broad use because of: (1) high specific energy and power densities [5,6]; (2) high nominal voltage and low self-discharge rate [7]; and (3) long cycle-life and no memory effect [8]. However, lithium-ion batteries must be precisely observed and managed (electrically and thermally) to avoid safety (inflammability) and performance related issues [9,10].

This section gives a brief overview of lithium-ion battery structure, components and types. A lithium-ion battery cell usually has five distinctive layers, in particular: the negative current collector, negative electrode (anode), separator, positive electrode (cathode), and positive current collector. There are generally four sorts of positive electrode materials [11]: (a) a metal oxide with layered structure, for example, lithium cobalt oxide ($LiCoO_2$/LCO) [12]; (b) a metal with a three dimensional spinal structure, for example, lithium manganese oxide ($LiMn_2O_4$) [13]; (c) lithium nickel manganese cobalt oxide ($LiNiMnCoO_2$/NMC); and (d) a metal with a olivine structure, such as lithium iron phosphate ($LiFePO_4$/LFP) [14]. The anode is generally made of graphite or a metal oxide. The electrolyte can be liquid, polymer or solid. There are various types of lithium-ion batteries available such as cylindrical, and prismatic. The prismatic batteries are used for high capacity rating such as in automobiles [15].

In EVs and HEVs, the thermal management of lithium-ion batteries is a tremendous challenge because of the dynamic utilization of the battery cells and the extensive range of environments under which they work [16]. In a high temperature environment, lithium-ion batteries quickly degrade, while in a cold temperature environment, the power

* Corresponding author.
E-mail addresses: satyam.panchal@uwaterloo.ca, satyam.panchal@uoit.ca (S. Panchal).

https://doi.org/10.1016/j.epsr.2018.05.020
Received 7 February 2017; Received in revised form 23 February 2018; Accepted 22 May 2018
Available online 30 May 2018
0378-7796/

Nomenclature

e	e is the number also called as Napier's Number and its approximate value is 2.718281828
H_k^1 *to* H_k^8	Hidden layer neuron from 1 to 8
I	Current [A]
i	Index of hidden layer nodes
j	Index of input layer nodes
k	Index of time interval
l	Index of output layer nodes
N_H	Number of neurons in the hidden layer
N_I	Number of neurons in the input layer
N_o	Number of neurons in the output layer
t	Time [s]
$W_{i,j}$	Weights of connection between hidden layer neuron and output layer neurons
x	Weighted sum of inputs from the preceding layers
β_1 *to* β_8	Bias of hidden layer neurons from 1 to 8
Γ	Average temperature of all 20 module
θ_k	Time recorded from EV in second
μ	Bias associated with the output layer neuron
ξ_k	Battery current recorded from EV in Amp
π	Pi
$\sigma(.)$	Activation function
$\omega_{i,j}$	Weights of connection between input layer neuron and hidden layer neurons
∞	Infinity

Subscripts

act	Actual
chg	Charge
dis	Discharge
int	Internal
sim	Simulated
oc	Open circuit
out	Output

Superscripts

T	Transpose of a matrix
x	power value of the exponent e

Acronyms

ANN	Artificial neural network
BC	Boundary condition
BMS	Battery management system
BTMS	Battery thermal management system
C	Capacity
CC	Constant-current
CV	Constant-voltage
DAQ	Data acquisition
EV	Electric vehicle
FCV	Fuel cell vehicle
IFR 18650	"I" stands for Li-ion rechargeable, "F" stands for the element "Fe" which is Iron, "R" just means the cell is round, 18650 means 18 mm diameter and 650 means 65 mm height
$LiCoO_2$	Lithium cobalt oxide
$LiMn_2O_4$	Lithium manganese oxide
$LiNiMnCoO_2$	Lithium manganese cobalt oxide
$LiFePO_4$	Lithium iron phosphate
LCO	Lithium cobalt oxide
LFP	Lithium phosphate
LPM	Lumped parameter model
LPV	Linear parameter varying
LM-ANN	Levenberge–Marquardt artificial neural network
MSE	Mean square error
NN	Neural network
NMC	Lithium manganese cobalt oxide
OCP	Open circuit potential
PSAT	Power train system analysis tool kit
PHEV	Plug-in hybrid electric vehicle
PDE	Partial differential equation
R	Regression
RS-232	Recommend standard number 232
SOC	State of charge
TDI	Load box for battery testing
UQM	Power phase motor developed by UQM

output and energy are reduced, which eventually brings about reduction of performance and driving range [17]. A typical temperature range is between 20 °C and 40 °C [18] for lithium-ion batteries, and an extended range is between −10 °C and +50 °C for their fair operation [16]. There are two common types of cooling: (i) air cooling, and (ii) water cooling. The water cooling option appears to be more compelling, because of higher specific heat content contrasted with air cooling. It occupies less volume, yet brings more complexities and high cost and weight [19]. The temperature increase in a lithium-ion battery during charging/discharging follows three processes: (1) the rate at which heat is created inside the cell, (2) the rate at which heat conducts within the cell to the outer surface, and (3) the rate at which heat is expelled from the cell's external surface to the environment. Heat dissipation to the surrounding relies on the cell geometry and also the cooling system performance [20]. Temperature estimations and the prediction of the lithium-ion cell temperature are addressed by various papers including analytical and numerical modeling [21,22].

Numerous numerical models have been developed to predict the dynamic behaviors of batteries. An EV designer may use battery models for sizing the required battery and predict the battery discharge. Battery models are likewise utilized for on-line self-learning performance and SOC estimation in battery thermal management system (BTMS) [23,24]. There are numerous papers in the open literature available for battery thermal modeling, utilizing diverse methodologies. For example, artificial neural network [21,22,25,26], finite element model (FEM) [27] or lumped parameter model (LPM) [28], the linear parameter varying (LPV) model [29], or the partial differential equation (PDE) model [30], and the power train system analysis toolkit (PSAT) or Autonomie [31]. Some more studies on SOC estimation based on drive cycles are also accessible in the open literature [32,33]. Utilizing smart tools, for example, artificial neural networks (ANNs) has ended up being effective tools for exact estimating of vehicle pace profile of moving vehicle. A neuro-genetic predictive tool was produced for predicting the short-term traffic activity on road [34]. Genetic algorithm (GA) was also additionally utilized for the both optimization and developing of ANN architectures for short-term traffic flow prediction [35]. An ANN in view of an exponential smoothing strategy was produced to come up with a precise intelligent tool for forecasting the traffic flow, and later confirmed the realness of their system by repeating the same simulations using a Levenberge-Marquardt ANN (LM-ANN) [36]. In another study, a neural network for real-time vehicle speed predictions showed the legitimacy of the strategy utilized [37]. Here, we used the same methodology called ANN for drive cycle modeling. Artificial neural networks are generally sorted out in layers

with nodes or neurons connecting different layers through an activation function. Data or patterns are presented at the input layer which travels to the hidden layers through weighted connections and lastly processed at the output layer which represents the output of the network.

Note that there are various algorithms to train a neural network, such as: (i) the gradient descent, which is also known as steepest descent, is the simplest training algorithm, requires information from the gradient vector, and hence it is a first order method. It has a severe drawback of requiring many iterations for functions, which have long, narrow valley structures. This is recommended when there are big neural networks, with many thousands of parameters. (ii) The Newton's method is a second order algorithm with an objective which aims to find better training directions by using the second derivatives of the loss function. This is quite expensive in computational terms. (iii) The conjugate gradient method can be regarded as intermediate between gradient descent and Newton's method. This method is more effective than gradient descent in training networks and is recommended when there are big neural networks. (iv) The quasi-Newton or variable metrix methods are known as computationally expensive. This method is faster than both gradient descent and conjugate gradient methods. (v) The Levenberg–Marquardt algorithm is known as a method tailored for functions of the type sum-of-squared-error which makes it very fast when training neural networks measured on that kind of errors.

Undertaking both experimental investigation and simulation studies are absolutely much demanded and that is what the present work did. In addition, a comprehensive investigation and simulation is conducted on the lithium-ion battery performance under different drive cycles with various boundary conditions (BCs) or ambient temperature of 2 °C, 10 °C and 17 °C, and the performance is assessed in such a manner. Furthermore, we designed and developed an experimental facility which is capable of testing different types of batteries with different kinds of chemistries. To the best of the authors' knowledge no similar studies on a prismatic lithium-ion battery have been reported in the open literature. This study comprises following specific objectives:

- Design and development of test bench experimental system and testing of collected drive cycles.
- Development of the battery thermal model using ANN and validation with the road test data.
- Performance assessment and evaluations under various drive cycles into test bench.
- Comparison and validation studies for EV real world drive cycles collected at different ambient temperatures.

2. Experimental set-up

In this section, the vehicle and experimental details are provided through a description of the test vehicle, a data logger, battery pack or module, experimental set-up, battery, thermocouple sensor locations, and thermal data acquisition system.

Table 1
Key specifications for the EV.

Specification	Value
Mass (empty)	1814 kg
Motor peak power	125 kW
Motor peak efficiency	98% at 4000 RPM
Motor peak torque	239 Nm
Battery module nominal voltage	19.2 V
Battery module energy density	89 Wh/kg
Battery module nominal capacity	69 Ah
Total battery pack energy capacity	25 kWh
Typical range for full SOC swing	100 km
Time 0-100 kilometers per hour (kph)	About 12 s

The EV used for this work is shown in Fig. 1(a) and the main features of the EV are displayed in Table 1. There are three battery packs of lithium-ion battery installed on the vehicle, including a total of 20 battery modules in series. Every module contains 6 series × 49 parallel IFR 18650 Cylindrical Valence cells, i.e., every battery module incorporates 6 strings of battery cells in series and each string contains 49 cells in parallel resulting in an aggregate of 294 cells in every battery module. The cells utilized as a part of this EV are 18650 cylindrical cells in configuration and their specifications are shown in Table 2. The first six modules are associated in series arrangement and are shown in Fig. 1(b). Note that these are inside the first battery pack at the front side of the vehicle. The ISAAC data logger is installed in the vehicle underneath the front passenger seat. The cellular antenna that enables wireless data transmission is located on top of the car. The data logger is powered by the existing 12 V battery in the vehicle. The EV has a 125 kW UQM power phase electric motor beneath the front battery pack.

The drive cycles obtained from the EV were conducted in a hybrid test bench in the lab as shown in Fig. 2(a). It was originally built to test various hybrid technologies as well as assess their usefulness in vehicle design. Notwithstanding, the hybrid test bench was adjusted to test batteries on various duty cycles and to quantify battery thermal performance and degradation. The test bench comprises a PC for charge/discharge information, load box, power supply, and a battery management system (BMS). The low voltage supply and load were Lambda ZUP20-40-800 and TDI Dynaload RBL323-50-150. The data acquisition (DAQ), known as BMS, as it appears on the right hand side of Fig. 2(a), is utilized as a part of the tests to log the battery electrical data and thermal data. The BMS is utilized to log the battery electrical data, including time, charge current, discharge current, charge voltage, and discharge voltage, and for the thermal data, including temperature. Both the electrical and thermal data were recorded at regular intervals of one second.

In EV applications, the battery system comprises of various single

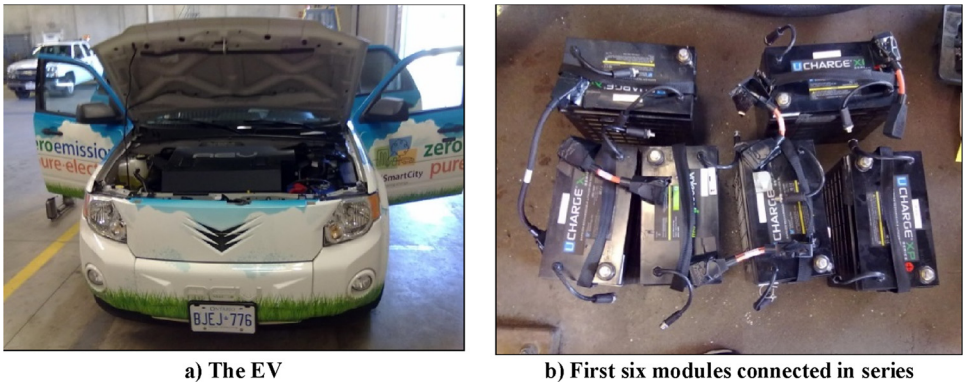

a) The EV b) First six modules connected in series

Fig. 1. The EV and first six modules connected in series.

Table 2
EV cell specification.

ESS specification, valence IFR18650e	Value
Number of battery packs	3
Number of modules	20
Number of cell per module	6 in series
Charge voltage	3.65 V standard (3.4 V float, 4.2 V max)
Nominal operating voltage	3.2 V
Nominal rated capacity (C/5)	1350 mAh (1.4 Ah)
Discharge cut-off voltage	2.5 V
Cell dimensions	Length: 65 mm, diameter :18.2 mm
Cell weight	40 g

cells connected either in a series or a parallel arrangement, keeping in mind the end goal to achieve the power and capacity requirements. The pack, as it appears in Fig. 2(b), consists of four cylindrical 18650 lithium-ion cells electrically connected in series. As explained in the previous paragraph, the pack was instrumented with T-type thermocouples, as well as a pack current and individual cell voltage sensor. In this series, each battery cell was experimentally characterized, so as to predict the cell voltage and capacity during discharging and charging operations at an ambient temperature (~22 °C). In all the conducted tests, the cells were first charged, and then used until totally discharged. The output voltage of the series connected cells and the discharge current are given by the equations below. It is very clearly understood that the temperature distribution is not uniform in a battery pack. Therefore, the operating temperatures of the cells are different from one another:

$$V_{out} = V_{cell1} + V_{cell2} + ...+V_{celln} \quad (1)$$

$$I_{out} = I_{cell1} = I_{cell2} = ...=I_{celln} \quad (2)$$

The internal resistance (r_{int}) can also be calculated based on the Ohm's law (covering the voltage drop divided by current values and the voltage drop is the difference between the open circuit voltage and the actual or measured terminal voltage) as given by:

$$r_{int} = \frac{\Delta V}{I} = \frac{V_{oc} - V_{act}}{I} \quad (3)$$

3. ANN model description

Using the ANN approach, a battery model is developed for voltage, SOC and temperature simulations based upon the information gained (time, voltage, current, temperature, SOC, and charge/discharge cycle) from the EV. The ANN architecture for the battery model is shown in Fig. 3(a). A total of 81,821 samples were considered for this model, out of which 70% samples (57,271) were utilized for training the model. Also, 15% samples (12,271) were utilized for validation and, finally, 15% samples (12,271) were utilized for testing the model. While the selected number of hidden neurons is eight, there are two inputs to the model: (1) driving time and (2) EV battery current. These two inputs are particularly chosen since they have a great impact on the entire performance of the battery during discharge. Here, the average temperature of all 20 modules is a function of EV driving time and EV battery current, which is given by:

$$\Gamma = f(\theta_k, \xi_k) \quad (4)$$

The number of hidden neurons is eight in light of the fact that the regression value is close to one at these neurons. As mentioned above, there are various strategies for training the algorithm: (1) the Levenberg–Marquardt method; (2) the Bayesian Regularization method; (3) the scaled conjugate gradient method; (4) Newton's method; and (5) the quasi Newton method. For training the model, the Levenberg–Marquardt Method was utilized as the default training algorithm for the feed-forward network in many commercial solvers, including MATLAB, due to its powerful nature. This calculation takes more memory, however less time. It automatically trains when generalization stops improving, as indicated by an increase in the mean square error (MSE) of the validation samples. The model was trained several times until the MSE is minimal and regression value (R) is near one, which implied that there is a close relationship between the targets and outputs. Here, in this model, the R value is 0.99896.

For the input training data, there are essentially two inputs to the model: the driving time and the EV battery current. For the output training data, in the output file, there is one output for the temperature, SOC or voltage. The experimental data are measured with a sampling period of 1 second. The regression plot is shown in Fig. 3(b), which demonstrates the regression relation between the actual output and the targets. When the MSE is low, the model is better. The corresponding data sets for MSE, R, and R^2 for all outputs is given in Table 3. The coefficient of determination (R^2) is the ratio between the expected and total variations. It is then given by

$$R^2 = \frac{Sum\ of\ expected\ variations}{sum\ of\ total\ variations} = \frac{\sum (\hat{Y}_i - \overline{Y})^2}{\sum (Y_i - \overline{Y})^2} \quad (5)$$

where $\overline{Y}$ is the mean of all observations, $\hat{Y}_i$ is the estimated observation at time i and Y_i is the actual observations. The value of R^2 ranges from 0 to 1. The nearer the value of R^2 is to 1, the better the observations fit with the selected forecasting model.

The error histogram showing the difference between the actual and the target output is plotted as shown in Fig. 4. Among the total samples

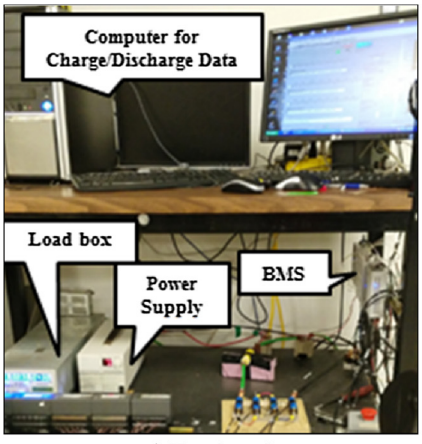

a) Test bench

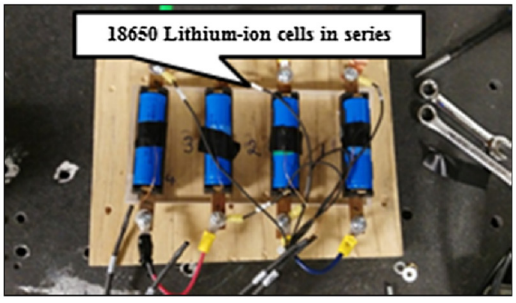

b) Lithium-ion 18650 cells connected in series

Fig. 2. Picture of test bench and lithium-ion 18650 cells connected in series.

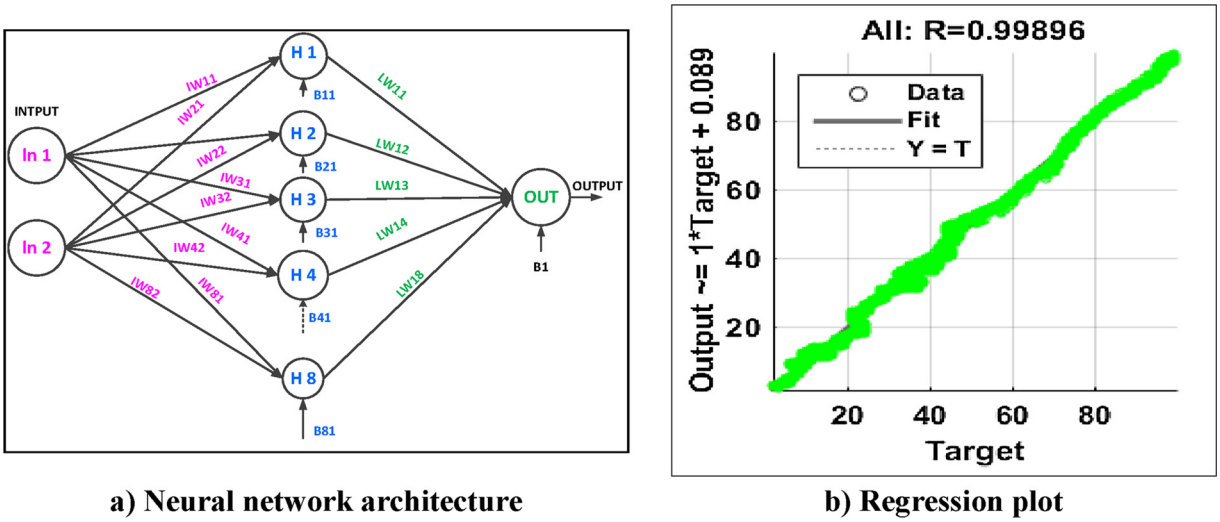

a) Neural network architecture b) Regression plot

Fig. 3. Neural network architecture and the regression plot.

Table 3
Mean square error and regression.

Outputs	MSE	R	R^2
0	2.3524	0.9887	0.9776
1	1.6191	0.9922	0.9845
2	0.7937	0.9962	0.9924
3	0.8192	0.9961	0.9922
4	1.2981	0.9938	0.9876
5	0.5859	0.9972	0.9944
6	0.8319	0.9960	0.9920
7	0.4470	0.9978	0.9957
8	0.4236	0.9979	0.9959

considered, the majority of errors lie in the range of -0.38 to 0.52. The activation functions are used in the network to scale the data output from a layer. Some commonly used activation functions in neural networks are listed as follows:

1) Log sigmoid function: The sigmoid function is given below. The function is real valued and differentiable, characterized by horizontal asymptotes as $x \rightarrow \pm \infty$

$$\sigma(x) = \frac{1}{1 + e^{-x}} \tag{6}$$

where $\sigma(.)$ is the activation function and x is the weighted sum of inputs from the preceding layers. Here, $\sigma(x) = 0$ when $x \rightarrow -\infty$, and $\sigma(x) = 1$ when $x \rightarrow \infty$.

2) Tan sigmoid function: This function is represented by

$$\sigma(x) = \frac{2}{1 + e^{-2x}} - 1 \tag{7}$$

In the above equation, $\sigma(x) = -1$ when $x \rightarrow -\infty$, and $\sigma(x) = 1$ when $x \rightarrow \infty$. This function can also be represented by a hyperbolic tan function by:

$$tanh \text{ or } \sigma(x) = \frac{e^{x} + e^{-x}}{e^{x} - e^{-x}} \tag{8}$$

The previous Equation (8) can also be represented as

$$tanh \text{ or } \sigma(x) = \frac{2}{\pi} arctan(x) \tag{9}$$

With the specific end goal to acquire a mathematical function of the average temperature of all 20 modules, Γ from the trained ANN, the output from each hidden layer neuron H_k^1 *to* H_k^8 is first determined. The incoming inputs with suitable weights $\omega_{i,j} \forall_i \in 1,\ldots, N_H$, $J \in 1 \ldots N_I$, are summed up at each hidden layer neuron. Moreover, each hidden layer neuron has additional input, the bias β_1 *to* β_8, which is used in the network to generalize the solution and to avoid a zero value of the output, even when an input is zero. This summed signal is passed through an activation function (tansig) associated with each hidden

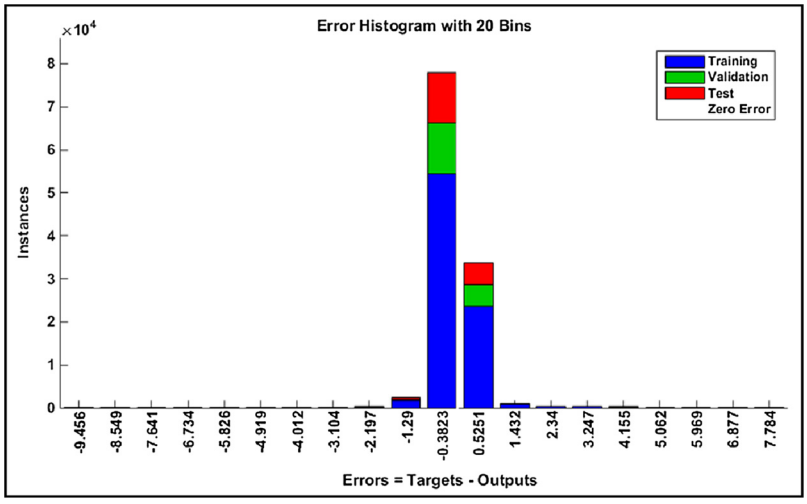

Fig. 4. Error histogram showing the difference between the actual and the target output.

layer neuron, which transforms the net weighted sum of all incoming signals into an output signal from the hidden layer neuron. H_k^1 *to* H_k^8 are given by

$$H_k^1 = tansig(\omega_{1,1}\theta_k + \omega_{1,2}\xi_k + \beta_1 \quad (10)$$

$$H_k^2 = tansig(\omega_{2,1}\theta_k + \omega_{2,2}\xi_k + \beta_2 \quad (11)$$

$$H_k^3 = tansig(\omega_{3,1}\theta_k + \omega_{3,2}\xi_k + \beta_3 \quad (12)$$

$$H_k^4 = tansig(\omega_{4,1}\theta_k + \omega_{4,2}\xi_k + \beta_4 \quad (13)$$

$$H_k^5 = tansig(\omega_{5,1}\theta_k + \omega_{5,2}\xi_k + \beta_5 \quad (14)$$

$$H_k^6 = tansig(\omega_{6,1}\theta_k + \omega_{6,2}\xi_k + \beta_6 \quad (15)$$

$$H_k^7 = tansig(\omega_{7,1}\theta_k + \omega_{7,2}\xi_k + \beta_7 \quad (16)$$

$$H_k^8 = tansig(\omega_{8,1}\theta_k + \omega_{8,2}\xi_k + \beta_8 \quad (17)$$

The weight matrix connecting the input layer neurons to the hidden layer neurons, i.e. $\omega_{i,j}\ \forall_i \in 1,\ldots, N_H, J \in 1,\ldots, N_I$ is given by

$$\omega_{i,j} = \begin{bmatrix} -1.4553 & 0.0407 \\ 5.0488 & 0.6065 \\ -12.6462 & -0.0778 \\ 17.9746 & -0.1370 \\ -1.1738 & 2.0517 \\ 1.2520 & -0.0439 \\ -1.2398 & 2.0596 \\ -13.2038 & -0.0778 \end{bmatrix} \quad (18)$$

The bias $\beta_i \forall_i \in 1,\ldots, N_H$, associated with each hidden layer neuron, is given by

$$\beta_i = [-0.7496 \quad -3.6840 \quad 3.7320 \quad 4.1838 \quad -0.4161 \quad 0.6783 \quad -0.4390 \quad 3.8915]^T \quad (19)$$

Finally, Γ can be obtained from the output neuron of the trained NN

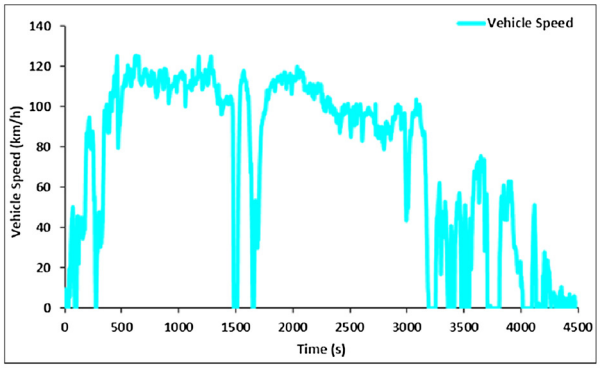

a) Drive cycle # 1

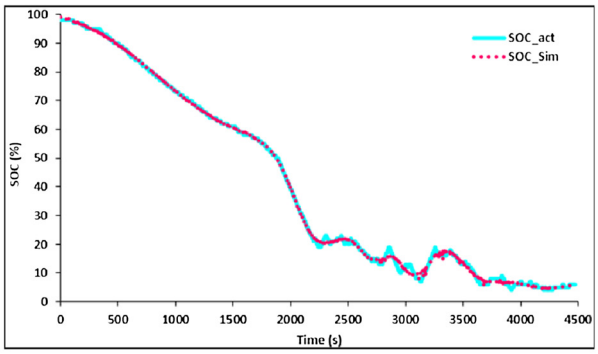

b) SOC profile for drive cycle # 1

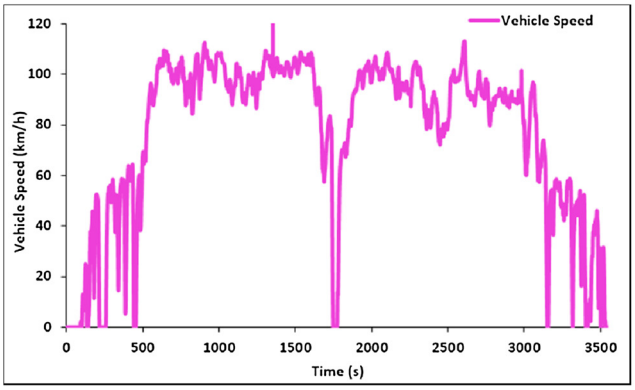

c) Drive cycle # 2

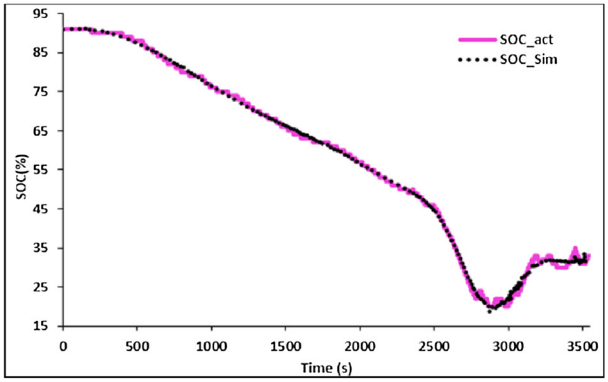

d) SOC profile for drive cycle # 2

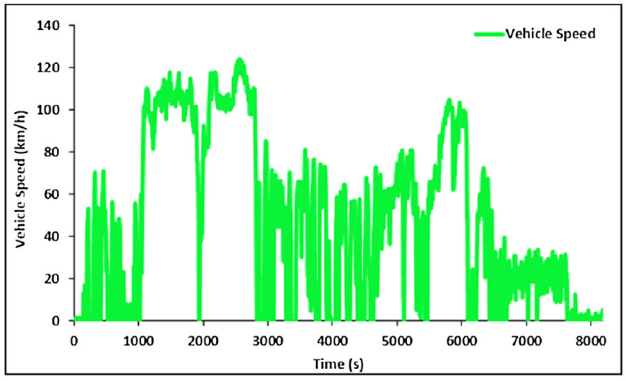

e) Drive cycle # 3

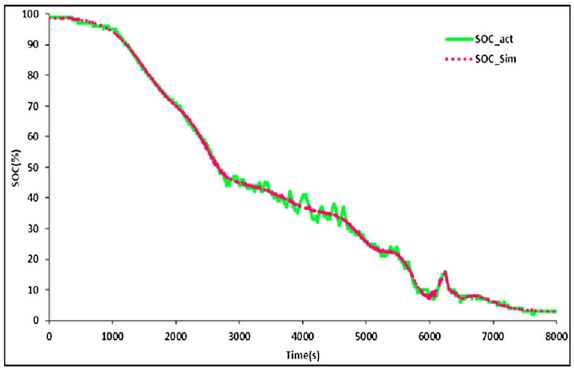

f) SOC profile for drive cycle # 3

Fig. 5. Details of drive cycles # 1, 2 and 3 and their corresponding battery SOC profiles.

as follows by

$$\Gamma = purelin(H_k^1 W_{1,1} + H_k^2 W_{1,2} + H_k^3 W_{1,3} + H_k^4 W_{1,4} + H_k^5 W_{1,5} + H_k^6 W_{1,6} + H_k^7 W_{1,7} + H_k^8 W_{1,8} + \mu \quad (20)$$

where, *purelin* is a linear transfer function available in MATLAB. The weight matrix connecting the hidden layer neurons with the single output neuron $W_{i,l} \forall_i \in 1,\ldots,N_H$, $l \in 1,\ldots, N_o$ is given by

$$W_{i,l} = [14.3878 \quad -0.2550 \quad 8.2288 \quad 0.0999 \quad 1.4017 \quad 14.7792 \quad -1.3659 \quad -7.8719] \quad (21)$$

and the bias associated with the output layer neuron is given by

$$\mu = -0.6202 \quad (22)$$

4. Results and discussion

After the information collected from the EV, the experiments done inside lab and model development study depicted in the former, this section clarifies the outcomes acquired for a drive cycle and also for a particular prismatic lithium-ion battery.

4.1. Drive cycle # 1 results

Fig. 5(a) demonstrates drive cycle # 1 acquired from the EV and the statistics of the same drive cycle are introduced in Table 4. The vehicle was driven for 1 h and 14 min with a cumulative distance of 90 km and a battery state-of-charge range of 98%–4%. The peak speed was seen as 125.5 km/h and occurred while driving on expressway 401 in the Province of Ontario. The average speed was 73.01 km/h. During this trip, the outside temperature was 10 °C. This drive cycle # 1 incorporates both city and highway driving. In Fig. 5(a), the drive cycle #1 portion between 300 1500s and between 1700–3200s is identified with the aggressive driving on highway 401 and, in the same way; and the segment between 3200–4500s represents the city driving. All electrical accessories were operating during this trip.

4.2. The SOC results for drive cycle # 1

Fig. 5(b) demonstrates the SOC profile (solid line) obtained from the EV for drive cycle # 1. Here, we can see a SOC range between 98–4%. Fig. 5(b) additionally demonstrates a comparison of the measured (actual) SOC with the values anticipated by the model. Overall, Fig. 5(b) shows good agreement between the experimental and simulation data, which is characteristic of the accuracy of the present model. There is a great reduction in the SOC profile between 100% to around 20% because of the expressway driving. Each of the three battery packs consistently withdrew power, after which an increase and decrease in the SOC curve is observed due to the regenerative braking in city driving, which involves frequent starts and stops because of intersections.

4.3. The battery voltage results for drive cycle # 1

Fig. 6(a) demonstrates the comparison of the battery voltage profile obtained from drive cycle # 1 of an EV with the data from the model. Overall, Fig. 6(a) shows good agreement between the experimental and simulation data, which is indicative of the accuracy of the present model. However, slight discrepancies are observed and the actual values are slightly higher than the values predicted by the model. These discrepancies may be due to regenerative braking.

4.4. The temperature results for drive cycle # 1

Fig. 6(b) shows the temperature profile (solid line) obtained from the EV for drive cycle # 1. In this vehicle; there are a total of 20 modules, of which this plot is the average temperature. A model-experimental comparison for this particular drive cycle # 1 is found in Fig. 6(b), where the temperature reaches 41 °C toward the end of the drive cycle. The EV utilizes 20 passively cooled battery modules situated in three packaged locations on the vehicle. It is clear that these different locations cause significant differences in cell temperature over the drive cycle. These differences may cause differential cell ageing, which can be monitored. It can be likewise observed that there is an extraordinary change in temperature between 500–3500s. As a result, the vehicle was constant in operation and all three battery packs continuously generated heat.

4.5. The drive cycle # 2 results

Fig. 5(c) demonstrates drive cycle # 2 acquired from the EV and the statistics of the same drive cycle are exhibited in Table 4. The vehicle was driven for one hour with a trip distance of 76 km and a battery state-of-charge range of 91– 33%. The peak speed was observed as 121.5 km/h and the average speed was 76.86 km/h. During this trip, the outside temperature was 17 °C. This drive cycle # 2 includes the aggressive driving on highway 401. The corresponding SOC profile for drive cycle # 2 is exhibited in Fig. 5(d), while the voltage validation is shown in Fig. 6(c) and the temperature validation is shown in Fig. 6(d).

4.6. The drive cycle # 3 results

Fig. 5(e) demonstrates drive cycle # 3 acquired from the EV and the statistics of the same drive cycle are displayed in Table 4. The vehicle was driven for 2 h and 16 min with a trip distance of 106 km and the battery state-of-charge was 100–2%. The peak speed was observed as 125 km/h while driving on the highway. The average speed was 46.9 km/h. During this trip, the outside temperature was 2 °C. This drive cycle # 3 incorporates both aggressive and gentle driving. The corresponding SOC profile validation for drive cycle # 3 is displayed in Fig. 5(f), while the voltage validation is shown in Fig. 6(e), and the temperature validation appears in Fig. 6(f).

4.7. The drive cycles validation results

After running all drive cycles in the test bench unit, the next step is data validation. A comparison between the electrical power input from drive cycle # 3 and the electrical power output from the test bench (four series connected cells) is shown in Fig. 7. It can be seen that the output electrical power closely matches the measured or actual data obtained from driving. Fig. 8(a) demonstrates the individual cell voltage profile during this drive cycle #3. Likewise, Fig. 8(b) demonstrates the stack voltage profile for this pack. The voltage window for the stack voltage profile is 14.5 V–11 V.

Table 4
Details of drive cycles # 1, 2 and 3.

Specification	Drive cycle # 1	Drive cycle # 2	Drive cycle # 3
Trip duration (min)	74	59	136
Trip distance (km)	90	76	106
Starting SOC (%)	98	91	100
Ending SOC (%)	4	33	2
Cycle average speed (km/h)	73.01	76.86	46.92
Cycle peak speed (km/h)	125.5	121.5	125
Average positive acceleration (m/s^2)	0.60	0.60	0.59
Peak positive acceleration (m/s^2)	3.93	3.01	3.43
Outside temperature (°C)	+10	+17	+2

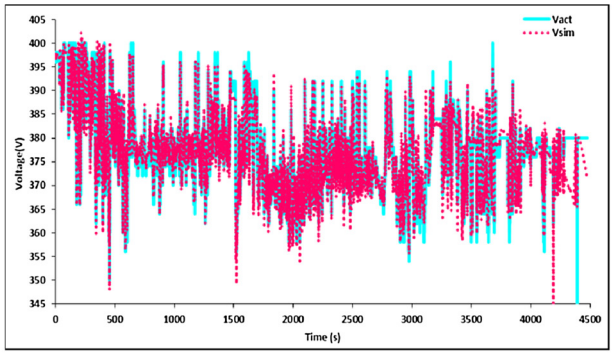

a) Battery voltage profile for drive cycle # 1

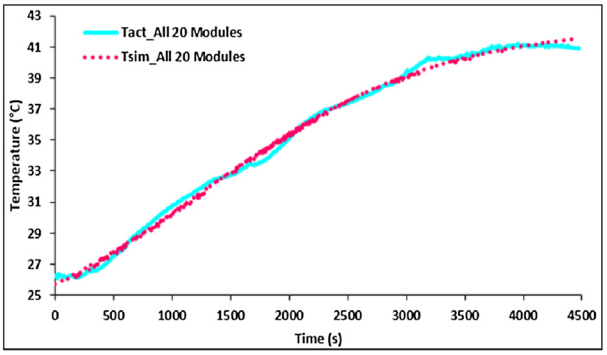

b) Temperature profile for drive cycle # 1

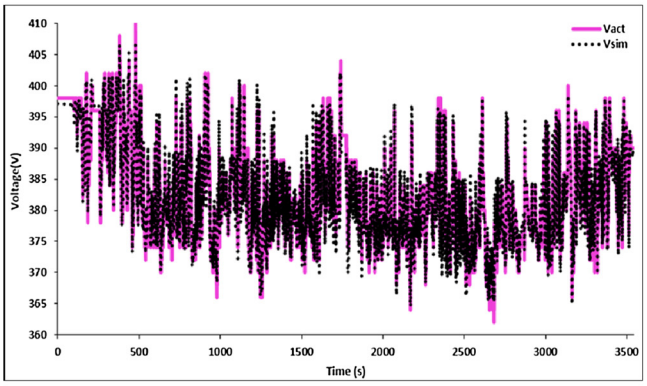

c) Battery voltage profile for drive cycle # 2

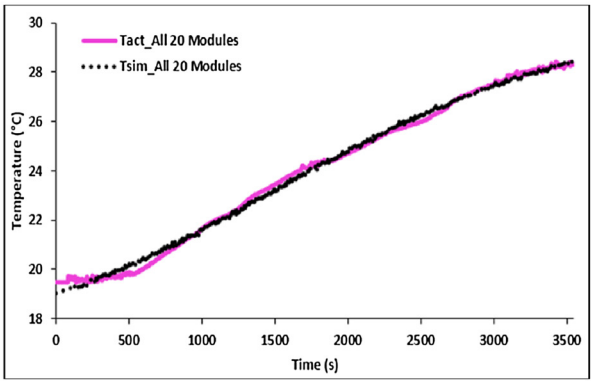

d) Temperature profile for drive cycle # 2

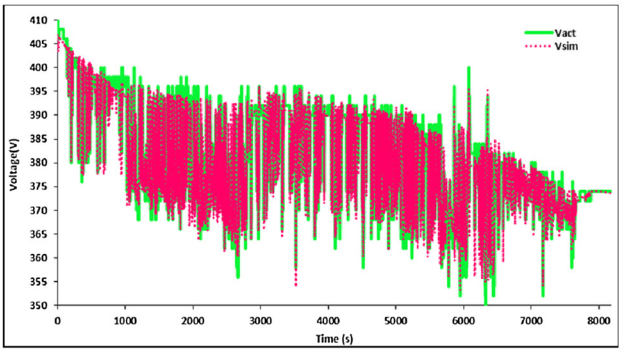

e) Battery voltage profile for drive cycle # 3

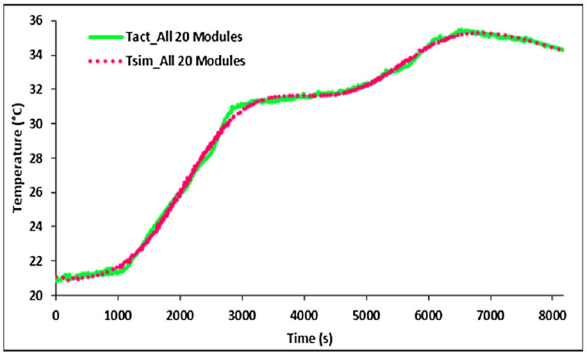

f) Temperature profile for drive cycle # 3

Fig. 6. Battery voltage profile and average temperature profile for all 20 modules for drive cycle # 1, 2 and 3.

Later on, the temperature profile obtained from the experimental data and real-world drive cycles were studied. The average battery surface temperature profile from experiment was almost close to the surrounding laboratory temperature. The temperature profile obtained from the real drive cycle # 3 is much higher, and does not follow the same trend. This was expected because of three main reasons: (1) the free convection from air in the laboratory has higher heat transfer rate than the battery installation in the EV module permits, (2) the ambient temperature in the lab was ~22 °C, while the real drive cycle was tested in November when the average ambient temperature was 2 °C, and (3) the EV has a thermal controller which activates fans automatically and is designed to maintain the pack temperature below certain point (~ 40 °C) regardless of the ambient temperature.

5. Conclusions

In this paper, both experimental and theoretical performance assessments of a lithium-ion battery pack using real world drive cycles from an electric vehicle are presented. The battery model is developed using artificial neural networks, which are validated with the real world drive cycles in terms of voltage, state of charge (SOC), and temperature profiles. The mathematical functions are also developed and presented with the weight and bias values. For this, three distinctive drive cycles were purposefully obtained at different ambient temperatures in order to measure the thermal and electrical performance of the battery modules. Furthermore, the statistical data analysis is carried out for the collected drive cycles and presented in the paper. The developed battery model is then validated in terms of the battery SOC, voltage, and temperature profiles of all 20 modules. It was found that the developed model effectively captured the charge/discharge behaviour over a wide variety of ambient conditions. The maximum temperature is found to be 41°C from all three reported drive cycles. Note that future work will concentrate on a more thorough thermal testing of real world drive cycles under controlled boundary conditions of −5 °C, −15 °C, and −25 °C. This will be done with the end goal of studying the impact of the discharge on the performance of the battery.

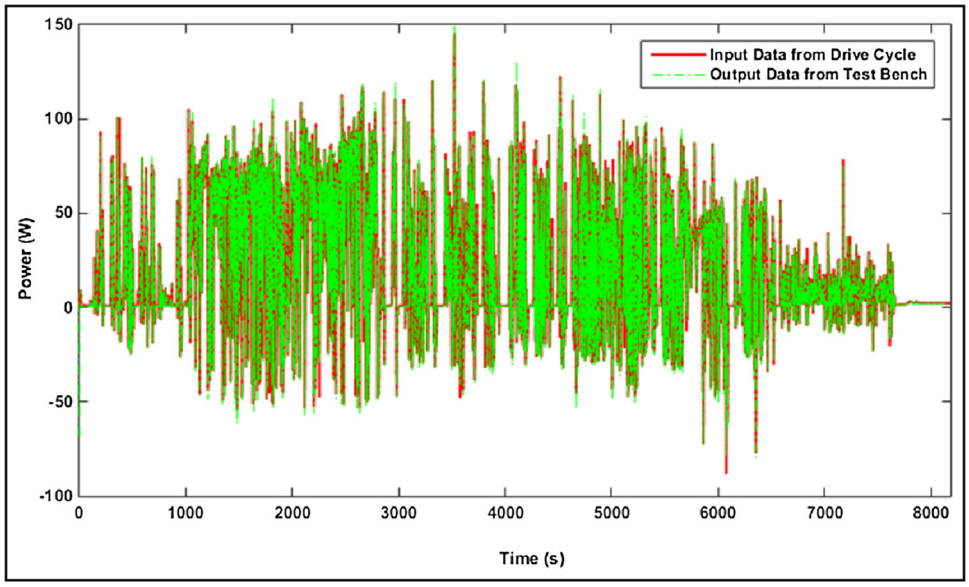

Fig. 7. Power profile for drive cycle # 3.

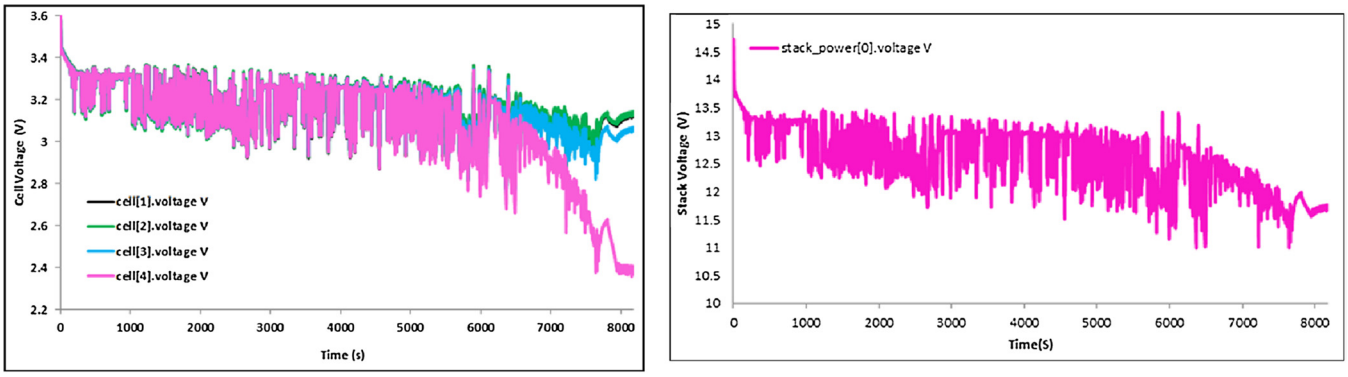

a) Cell 1,2,3,4 voltage profile for drive cycle # 3 **b) Stack voltage profile for drive cycle # 3**

Fig. 8. Cell 1,2,3,4 and stack voltage profile for drive cycle # 3.

References

[1] D. Chakraborty, W. Vaz, A.K. Nandi, Optimal driving during electric vehicle acceleration using evolutionary algorithms, Appl. Soft Comput. 34 (2015) 217–235.

[2] A.K. Nandi, D. Chakraborty, W. Vaz, Design of a comfortable optimal driving strategy for electric vehicles using multi-objective optimization, J. Power Sources 283 (2015) 1–18.

[3] A. Haddoun, M.E.H. Benbouzid, D. Diallo, R. Abdessemed, J. Ghouili, K. Srairi, Modeling, analysis, and neural network control of an EV electrical differential, IEEE Trans. Ind. Electron. 55 (6) (2008) 2286–2294.

[4] Q. Wang, Q. Sun, P. Ping, X. Zhao, J. Sun, Z. Lin, Heat transfer in the dynamic cycling of lithium–titanate batteries, Int. J. Heat Mass Transf. 93 (2016) 896–905.

[5] Z. Ling, F. Wang, X. Fang, X. Gao, Z. Zhang, A hybrid thermal management system for lithium ion batteries combining phase change materials with forced-air cooling, Appl. Energy 148 (2015) 403–409.

[6] H. Ge, J. Huang, J. Zhang, Z. Li, Temperature-adaptive alternating current preheating of lithium-ion batteries with lithium deposition prevention, J. Electrochem. Soc. 163 (2) (2016) A290–A299.

[7] A. Ritchie, W. Howard, Recent developments and likely advances in lithium-ion batteries, J. Power Sources 162 (2006) 809–812.

[8] Y. Ye, L.H. Saw, Y. Shi, A.A. Tay, Numerical analyses on optimizing a heat pipe thermal management system for lithium-ion batteries during fast charging, Appl. Therm. Eng. 86 (2015) 281–291.

[9] X. Feng, M. Fang, X. He, M. Ouyang, L. Lu, H. Wang, M. Zhang, Thermal runaway features of large format prismatic lithium ion battery using extended volume accelerating rate calorimetry, J. Power Sources 255 (2014) 294–301.

[10] L. Lu, X. Han, J. Hua, M. Ouyang, J. Li, A review on the key issues for lithium-ion battery management in electric vehicles, J. Power Sources 226 (2013) 272–288.

[11] K. Yeow, M. Thelliez, H. Teng, E. Tan, Thermal analysis of a Li-ion battery system with indirect liquid cooling using finite element analysis approach, SAE Int. J. 1 (1) (2012) 65–78.

[12] L.Y. Shao-Horn, C. Delmas, C.E. Nelson, M.A. O'Keefe, Atomic resolution of lithium ions in $LiCoO_2$, Nat. Mater. 2 (2003) 464–467.

[13] C. Julien, Local structure of lithiated manganese oxides, Solid State Ionics 177 (2006) 11–19.

[14] J.T. Bloking, S.Y. Chung, Y.M. Chiang, Electrically conductive phospho-olivines as lithium storage electrodes, Nat. Mater. 1 (2002) 123–128.

[15] J. Yi, U.S. Kim, C.B. Shin, T. Han, S. Park, Three-dimensional thermal modeling of a lithium-ion battery considering the combined effects of the electrical and thermal contact resistances between current collecting tab and lead wire, J. Electrochem. Soc. 160 (3) (2013) 437–443.

[16] F. He, L. Ma, Thermal management in hybrid power systems using cylindrical and prismatic battery cells, Heat Transf. Eng. 37 (6) (2016) 581–590.

[17] B. Wu, V. Yufit, M. Marinescu, G.J. Offer, R.F. Martinez-Botas, N.P. Brandon, Coupled thermal–electrochemical modelling of uneven heat generation in lithium-ion battery packs, J. Power Sources 243 (2013) 544–554.

[18] H. Teng, Y. Ma, K. Yeow, M. Thelliez, An analysis of a lithium-ion battery system with indirect air cooling and warm-up, SAE Int. J. Passeng. Cars Mech. Syst. 4 (3) (2011) 1343–1357.

[19] G.-H. Kim, A. Pesaran, R. Spotnitz, A three-dimensional thermal abuse model for lithium-ion cells, J. Power Sources 170 (2) (2007) 476–489.

[20] S.J. Drake, M. Martin, D.A. Wetz, J.K. Ostanek, S.P. Miller, A. Jain, Heat generation rate measurement in a Li-ion cell at large C-rates through temperature and heat flux measurements, J. Power Sources 285 (2015) 266–273.

[21] S. Panchal, I. Dincer, M. Agelin-Chaab, R. Fraser, M. Fowler, Experimental and theoretical investigation of temperature distributions in a prismatic lithium-ion battery, Int. J. Thermal Sci. 99 (2016) 204–212.

[22] S. Panchal, I. Dincer, M. Agelin-Chaab, R. Fraser, M. Fowler, Thermal modeling and validation of temperature distributions in a prismatic lithium-ion battery at different discharge rates and varying boundary conditions, Appl. Therm. Eng. 96

(2016) 190–199.
[23] L. Lam, P. Bauer, E. Kelder, A practical circuit-based model for Li-ion battery cells in electric vehicle applications, Telecommunications Energy Conference (INTELEC), IEEE 33rd International (2011) 1–9.
[24] A. Ostadi, M. Kazerani, S.K. Chen, Optimal sizing of the energy storage system (ESS) in a battery-electric vehicle, Transportation Electrication Conference and Expo (ITEC), IEEE (2013) 1–6.
[25] L. Mozaffari, A. Mozaffari, N.L. Azad, Vehicle speed prediction via a sliding-window time series analysis and an evolutionary least learning machine: a case study on San Francisco urban roads, Eng. Sci. Technol. Int. J. 18 (2015) 150–162.
[26] S. Panchal, I. Dincer, M. Agelin-Chaab, R. Fraser, M. Fowler, Experimental and theoretical investigations of heat generation rates for a water cooled $LiFePO_4$ battery, Int. J. Heat Mass Transf. 101 (2016) 1093–1102.
[27] A. Pruteanu, B.V. Florean, G. Maria Moraru, R.C. Ciobanu, Development of a thermal simulation and testing model for a superior lithium-ion-polymer battery, Optimization of Electrical and Electronic Equipment (OPTIM), IEEE (2012) 947–952.
[28] C. Alaoui, Solid-state thermal management for lithium-ion EV batteries, IEEE Trans. Veh. Technol. 62 (1) (2013) 98–107.
[29] X. Hu, S. Asgari, S. Lin, S. Stanton, W. Lian, A linear parameter-varying model for HEV/EV battery thermal modeling, Energy Conversion Congress and Exposition (ECCE), IEEE (2012) 1643–1649.
[30] A. Smyshlyaev, M. Krstic, N. Chaturvedi, J. Ahmed, A. Kojic, PDE model for thermal dynamics of a large, American Control Conference (ACC), IEEE (2011) 959–964.
[31] E. Samadani, S. Farhad, S. Panchal, R. Fraser, M. Fowler, Modeling and Evaluation of Li-ion Battery Performance Based on the Electric Vehicle Field Tests, SAE International 2014-01-1848, 2014.
[32] S. Cordiner, M. Galeotti, V. Mulone, M. Nobile, V. Rocco, Trip-based SOC management for a plugin hybrid electric vehicle, Appl. Energy 164 (2016) 891–905.
[33] B. Skugor, J. Deur, A novel model of electric vehicle fleet aggregate battery for energy planning studies, Energy 92 (2015) 444–455.
[34] W. Zheng, D. Lee, Q. Shi, Short-term freeway traffic flow prediction: Bayesian combined neural network approach, J. Transp. Eng. 132 (2) (2006) 114–121.
[35] E.I. Vlahogianni, M.G. Karlaftis, J.C. Golias, Optimized and meta-optimized neural networks for short-term traffic flow prediction: a genetic approach, Transp. Res. C: Emerg. Technol. 13 (3) (2005) 211–234.
[36] K.Y. Chan, T.S. Dillon, J. Singh, E. Chang, Neural-network-based models for short-term traffic flow forecasting using a hybrid exponential smoothing and Levenberg–Marquardt algorithm, IEEE Trans. Intell. Transp. Syst. 13 (2) (2012) 644–654.
[37] J. Park, D. Li, Y.L. Murphey, J. Kristinsson, R. McGee, M. Kuang, T. Phillips, Real time vehicle speed prediction using a Neural Network Traffic Model, The International Joint Conference on Neural Networks, San Jose, 2011.